Structure and performance of zeolite supported Pd for complete methane oxidation

(article starts on next page)

Structure and performance of zeolite supported Pd for complete methane oxidation

Ida Friberg [a], Adam H. Clark [b], Phuoc Hoang Ho [a], Nadezda Sadokhina [a], Glen J. Smales [c], Jungwon Woo [a], Xavier Auvray [a], Davide Ferri [b], Maarten Nachtegaal [b], Oliver Kröcher [b], Louise Olsson [a],[*]

[a] Chemical Engineering, Competence Centre for Catalysis, Chalmers University of Technology, SE-412 96, Gothenburg, Sweden
[b] Paul Scherrer Institut (PSI), Villigen, CH-5232, Switzerland
[c] Bundesanstalt für Materialforschung und -prüfung (BAM), Unter den Eichen 87, DE-12205, Berlin, Germany

ARTICLE INFO

ABSTRACT

The influence of zeolite support materials and their impact on CH_4 oxidation activity was studied utilizing Pd supported on H-beta and H-SSZ-13. A correlation between CH_4 oxidation activity, Si/Al ratio (SAR), the type of zeolite framework, reduction-oxidation behaviour, and Pd species present was found by combining catalytic activity measurements with a variety of characterization methods (operando XAS, NH_3-TPD, SAXS, STEM and NaCl titration). Operando XAS analysis indicated that catalysts with high CH_4 oxidation activity experienced rapid transitions between metallic- and oxidized-Pd states when switching between rich and lean conditions. This behaviour was exhibited by catalysts with dispersed Pd particles. By contrast, the formation of ion-exchanged Pd^{2+} and large Pd particles appeared to have a detrimental effect on the oxidation-reduction behaviour and the conversion of CH_4. The formation of ion-exchanged Pd^{2+} and large Pd particles was limited by using a highly siliceous beta zeolite support with a low capacity for cation exchange. The same effect was also found using a small-pore SSZ-13 zeolite due to the lower mobility of Pd species. It was found that the zeolite support material should be carefully selected so that the well-dispersed Pd particles remain, and the formation of ion-exchanged Pd^{2+} is minimized.

1. Introduction

Methane is a highly valued fuel and the main component in natural and biogas, however, it is also a greenhouse gas with a global warming potential 28 times higher than that of CO_2 over a 100-year period [1]. The emission of unburnt CH_4 from natural gas and biogas engines can be decreased through the oxidization of the CH_4 remaining in exhaust gas to CO_2. However, an efficient oxidation catalyst is required to operate under the typical temperature conditions found in an exhaust gas stream, as CH_4 is the most stable hydrocarbon. Pd-based catalysts have been shown to be the most efficient catalysts for the CH_4 oxidation reaction [2]. The kinetic rate limiting step under dry conditions is considered to be an abstraction of the first hydrogen atom, often referred to as the activation of the C–H bond [3,4].

The efficiency of the CH_4 oxidation of Pd-based catalysts is highly dependent on the oxidation state of Pd. The active phase for CH_4 oxidation is considered to be PdO [5–7]. However, some studies have proposed that a low amount of metallic Pd° can promote CH_4 oxidation, i.e. a mixed phase of PdO/Pd° is more active than PdO [8–11]. It has also been reported that the formation of oxidized Pd is accompanied with an increase in the level of CH_4 oxidation until a certain amount of PdO has been formed. At that point, any further formation of PdO has no discernible influence on the catalytic activity [7,12]. Murata et al. [13] have observed the highest level of CH_4 oxidation using support materials with moderate oxide formation enthalpy resulting in particles consisting of a metallic Pd core surrounded by a PdO shell. Consequently, the relationship between the oxidation state of Pd and CH_4 oxidation is complex. The oxidation process of Pd° is initiated by the quick chemisorption of oxygen onto the Pd° surface [6,7,14]. It is agreed that metallic Pd particles covered with chemisorbed oxygen exhibit some, but low, CH_4 oxidation activity [5,7,15]. The oxidation process of Pd proceeds by the dissolution of oxygen atoms into the Pd° core [14],

resulting in the slow formation of PdO with a high level of CH_4 oxidation [5,7,11,15]. PdO reduction can be accomplished at relatively low temperatures under CH_4-rich conditions. This makes it possible to study the relation between the oxidation state of Pd and low-temperature CH_4 oxidation activity using alternated rich (CH_4) and lean (O_2/CH_4) pulses [11,16,17]. The oxidation-reduction properties of Pd also depend on the catalyst composition, for instance, the choice of support materials. As an example, PdO formation is facilitated by using support materials with a high capacity to store oxygen [11] and low acidity [18,19]. The Pd°-to-PdO transition more readily occurs with small Pd particles. The reverse process of PdO decomposition is easier for larger particles because of the weaker interaction between oxygen and Pd in larger particles [14]. The strong Pd-O bonds in small crystallites (or those in closer contact with the support) has been suggested to explain the lower level of CH_4 oxidation of small PdO crystallites than of slightly larger PdO particles [4,20]. The identification of the active phases as well the mechanism for this reaction is complex and has been the subject of various experimental and theoretical studies [3,6,21,22].

Palladium supported on metal oxides, most commonly Al_2O_3, is one of the most thoroughly investigated catalysts for CH_4 oxidation. The Pd/ Al_2O_3 can also be promoted with ceria and other rare-earth elements (La, Pr, Tb) [23]. However, Al_2O_3 supported catalysts severely deactivate in the presence of water vapour, which typically constitutes approx. 10–15 % of the exhaust gas in natural gas combustion [2]. Zeolite-supported Pd has gained attention as a CH_4 oxidation catalyst, as it can be synthesized to provide high resistance against water deactivation [17,24–27]. For instance, the resistance to water deactivation can be significantly improved using low-aluminium zeolites as the Pd [24, 26] and Rh supports [28]. An increase in the SiO_2/Al_2O_3 ratio (SAR) is commonly accompanied by a higher conversion of CH_4 under dry conditions, which can be related to the formation of highly active PdO agglomerates, and the facilitated reduction and oxidation of Pd due to fewer ion-exchanged Pd^{2+} species [24,26]. It has been shown that the activity and stability of zeolite-supported Pd can be enhanced with the acid removal of extra-framework aluminium, the formation of mesopores upon desilication treatment, and with a decrease in acidity through full ion-exchange of the acidic sites with alkali metal cations [17,25]. Lim et al. [27] have compared various small-pore zeolites and the associated high activity of long-term CH_4 oxidation was attributed to less Pd sintering of catalysts with strong interactions between PdO and zeolite frameworks with high acidity. The complexity of zeolite-supported catalysts is influenced by many factors, such as zeolite framework, SAR, the type of cation exchanged with the zeolite Brønsted acid sites, and the character of the acid sites [17,24–27,29–31]. By using zeolites, Pd can form particles either on the external surface of the zeolite and/or internally within its pores. In addition, Pd can form ion-exchanged Pd species on Brønsted acid sites in the zeolite framework. The current literature indicates that ion-exchanged Pd^{2+} species provide a lower level of CH_4 oxidation than PdO particles [24,26,32,33], however, this should be confirmed with additional studies using detailed characterization methods. The formation of ion-exchanged Pd^{2+} species can be limited by using zeolites with high SAR [24,34]. The conditions for catalyst pre-treatment are another crucial factor for the formation of ion-exchanged Pd^{2+} species. The formation of ion-exchanged Pd^{2+} can be facilitated under lean conditions [29–32,35], at high temperatures, and for certain zeolite types, in the presence of water vapour [36–38].

Another complexity of zeolite-supported Pd catalysts is that Pd can rearrange to form large Pd° particles on the external zeolite surface under rich conditions and then re-disperse into small PdO species and/or monodispersed Pd ions under lean conditions [29–32,35]. The latter feature is more pronounced for zeolites with a high content of Al; however, the type of zeolite framework can also influence Pd speciation [29–31].

Although the benefits of using zeolites over traditional metal oxide support materials for Pd-based CH_4 oxidation catalysts have been demonstrated in the literature, there remain a number of open questions for these types of catalytic systems. The nature and distribution of the Pd species and their effect on catalytic activity remains a major and complex issue. Knowledge about this is essential to tailor the synthesis of highly efficient catalysts based on zeolite-supported Pd. The choice of zeolite support has a direct influence on the type of Pd species formed, which can strongly affect the level of CH_4 oxidation. By combining catalytic activity measurements with a variety of characterization techniques (XANES, EXAFS, NH_3-TPD, SAXS, STEM and NaCl-titration), we can correlate the level of CH_4 oxidation to the Si/Al ratio (SAR), the type of zeolite framework, and the reduction-oxidation behaviour and nature of Pd species.

2. Experimental

2.1. Catalyst preparation

Three catalyst samples were prepared with different support materials according to the methods described in our previous work [24]. One Pd/H-SSZ-13 (SAR = 43) sample and two Pd/H-beta samples (SAR = 40, 511) were prepared. The incipient wetness method was used to add 1 wt % of Pd to the support materials. The samples will be referred to hereinafter as PdB40 (Pd/H-beta, SAR = 40), PdB511 (Pd/H-beta, SAR = 511), and PdS43 (Pd/H-SSZ-13, SAR = 43). The highly siliceous beta zeolite PdB511 was chosen based on its high level of activity and stability in the presence of water as well as enhanced sulfur regeneration [24]. This catalyst was compared with low SAR Pd/zeolites (PdB40 and PdS43) to further understand its excellent properties.

It should be noted that the H-beta support used for the PdB511 sample was dealuminated with an oxalic acid solution prior to Pd deposition in order to increase its SAR. Details on the dealumination procedure are available in our previous work [24]. The contents of Pd, Al, and Si were measured with inductively coupled plasma sector field mass spectrometry (ICP-SFMS, performed by ALS Scandinavia AB) and are listed in Table 1. Parts of the prepared catalyst powders were washcoated onto cordierite monoliths (diameter=15 mm, length=20 mm) [24]. The final monoliths contained 300 mg (±5 mg) of washcoat (95 wt% catalyst powder, 5 wt% boehmite binder, Sasol Disperal P2) and were used for temperature-programmed desorption of NH_3 (NH_3-TPD). The other methods were performed using the catalyst powder as prepared.

A Pd/γ-Al_2O_3 reference sample was prepared and tested for comparison with the zeolite supported samples. The results for this sample are presented and discussed in Supplementary material (Figs. S11–15).

Table 1
Pd loading, SiO_2/Al_2O_3 molar ratio (SAR), and Pd/Al molar ratio from ICP-SFMS measurements.

	Sample	Pd loading (wt%)	SAR (SiO_2/Al_2O_3, molar ratio)	Pd/Al (molar ratio)
PdB511	Pd/H-beta	1.05	511	1.96
PdB40	Pd/H-beta	0.92	40	0.14
PdS43	Pd/H-SSZ-13	1.02	43	0.16

2.2. Characterization and catalytic activity measurements

2.2.1. X-ray absorption spectroscopy (XAS) and catalytic activity measurements

Transmission QuickEXAFS measurements were performed at the SuperXAS beamline [39] at the Swiss Light Source (SLS) using 15 cm long ion chambers filled with 1 bar N_2 and 1 bar Ar. A Pd foil mounted between the second and third ion chambers was used to calibrate internal energy. The storage ring was operated at 2.4 GeV in top-up mode with a ring current of 400 mA. The polychromatic X-ray beam resulting from a 2.9 T superbend magnet was collimated with a Pt-coated mirror and subsequently monochromatised with a Si(111) channel-cut monochromator. The resulting monochromatic X-ray beam was focused using a Pt-coated toroidal mirror to a spot size of ~150 × 150 μm.

A sieved powder fraction (100−150 μm) was loaded between two plugs of quartz wool in a plug-flow reactor cell equipped with 250 μm thick graphite windows [40]. The weights of the loaded samples were 24.1 mg (PdB40), 24.6 mg (PdB511), and 26.6 mg (PdS43). The outlet gases were detected with a mass spectrometer (MS, Omnistar, Pfeiffer). Prior to the rich-lean pulse experiments, the samples were degreened and pre-treated at 450 °C according to the protocol in Table 2. The samples were then cooled to 360 °C in 2 vol% O_2/Ar. This temperature was maintained while the catalyst powders were exposed to 2 vol% O_2/1000 ppm CH_4/Ar for 30 min. This was followed by a rich pulse (70 mL/min, 1430 ppm CH_4/Ar) for 1 min and then 9 min of lean conditions (100 mL/min, 2 vol% O_2/1000 ppm CH_4/Ar). The latter rich-lean pulse sequence was repeated 10 times, *i.e.* for a period of 100 min. This entire procedure, except for the degreening steps i-iv in Table 2, was then repeated at 330 °C, 300 °C, and 270 °C. After the pulse sequence at each temperature, the samples were cooled to the next temperature in 2 vol% O_2/Ar. The MS displayed sudden spikes in some of the gas concentration data. These spikes were caused by pressure fluctuations but did not influence the overall interpretation of the data.

X-ray absorption spectra were recorded at the end of the 30-min steady state CH_4 oxidation, during the first rich and lean pulse, and the two last cycles of rich-lean pulses. The measurements were acquired in transmission mode around the Pd K-edge (24.350 keV). The spectra were background corrected, normalized, and interpolated using Pro-QEXAFS data processing software [41]. The fraction of Pd^{2+} was determined with linear combination fitting (LCF) of the X-ray absorption near edge structure (XANES) spectra (24.250–24.450 keV) using the spectra of PdO and Pd° metal foil as references. The extended X-ray absorption fine structure (EXAFS) analysis was performed on the Fourier transformed k^2-weighted EXAFS spectra (k range 3.0–10.25 Å) using the DEMETER software package [42]. The amplitude reduction factor (S_0^2) was determined by fitting the first Pd-Pd coordination shell of a simultaneously collected Pd° foil. The pseudo Debye-Waller factor (σ^2) for the first Pd-Pd shell of metallic Pd was estimated with the Debye model using a Debye temperature (θ_D) of 274 K. The spectra of the oxidized Pd samples were fitted to three scattering paths, *i.e.* Pd-O, Pd-(O)-Pd1, and Pd-(O)-Pd2. The σ^2 and ΔR for these three shells were extracted from the fit of fully oxidized samples at each experimental temperature.

2.2.2. Temperature-programmed desorption of NH_3 (NH_3-TPD)

The acidity of the samples was evaluated with NH_3-TPD. NH_3 adsorption and desorption experiments were conducted using wash-coated monoliths and a flow reactor, described elsewhere [24], with a total flow of 800 mL/min (13 600 h^{-1}). The outlet gases were measured with a Fourier transform infrared (FTIR) spectrometer (MKS MultiGas 2030 HS FTIR). The monolith samples were first degreened and pre-treated according to Table 2 and subsequently cooled to 100 °C in 2 vol% O_2/Ar. This was followed by NH_3 adsorption in 500 ppm NH_3/Ar at 100 °C for 2 h. NH_3 was then removed from the feed, and the samples were flushed with Ar for 1.5 h. The TPD was subsequently conducted in Ar by heating from 100 °C to 500 °C at 10 °C/min.

2.2.3. Titration of ion-exchanged Pd^{2+}

The amount of ion-exchanged Pd^{2+} atoms was estimated with NaCl titration based on the method developed by Ogura et al. [43], demonstrating the high degree of ion-exchanged Pd^{2+} in Pd/ZSM-5 (98 %) compared to Pd/SiO$_2$ (0%), which was further verified with NO adsorption experiments. The sample powder used for this analysis was degreened, pre-treated (according to Table 2), and exposed to the experimental sequence at 360 °C (*i.e.* 30-min steady state CH_4 oxidation and 10 rich-lean pulse cycles). Sample powder (70 mg) was added to a 50 mL NaCl solution (0.1 M) at 80 °C and heated and stirred for 1 h. This step was repeated one more time after removing the liquid phase with centrifugation, *i.e.* the powder was ion-exchanged in NaCl solution twice. Finally, the powder was washed with milliQ water and dried at room temperature. The remaining Pd content in the sample after the NaCl process was determined with ICP-SFMS.

2.2.4. Particle size estimation

Pd particle size was studied with scanning transmission electron microscopy (STEM) and small- and wide-angle X-ray scattering (SAXS/WAXS). The powder used for these techniques was degreened, pre-treated, and exposed to the experimental sequence at 360 °C (*i.e.* 30-min steady state CH_4 oxidation and 10 rich-lean pulse cycles). The STEM images were obtained with a FEI Titan 80–300 microscope using an acceleration voltage of 300 kV. Small- and wide-angle X-ray scattering (SAXS/WAXS) measurements were performed with the MOUSE, a customised Xeuss 2.0 (Xenocs, France). X-rays were generated from a microfocus X-ray tube with a copper target, and a multilayer optic was employed to parallelise and monochromatize the beam to the Cu Kα wavelength of 0.1542 nm. The samples were examined as powders fixed between two pieces of Scotch Magic tape in the vacuum sample chamber. Data collection was performed using an in-vacuum Eiger 1 M detector (Dectris, Switzerland), which was placed at distances between 137–2507 mm from the sample. The resulting data was processed and scaled to absolute units using the DAWN software package according to
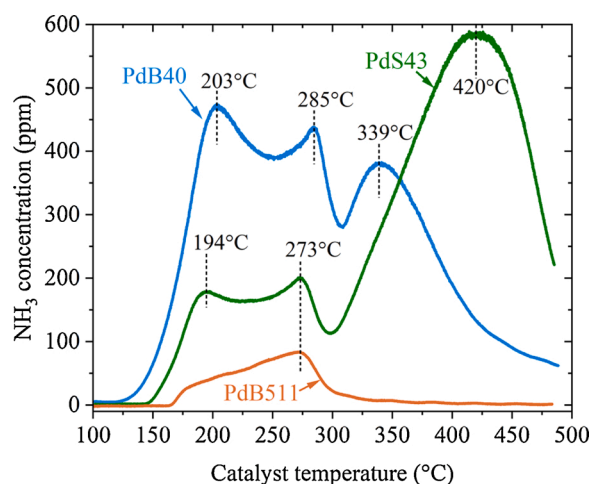
Table 2
Conditions for degreening and pre-treatment at 450 °C prior to the pulse operando XAS experiments.

Degreening	i) 2 vol% H_2/Ar, 20 min
	ii) 1000 ppm CH_4/2 vol% O_2/Ar, 10 min
	iii) 2 vol% H_2/Ar, 10 min
	iv) 1000 ppm CH_4/2 vol% O_2/Ar, 10 min
Pre-treatment	v) 2 vol% O_2/Ar, 20 min

Fig. 1. Temperature-programmed desorption of NH_3 (NH_3-TPD) for PdB511 (orange line), PdB40 (blue line), and PdS43 (green line) samples. (For interpretation of the references to colour in this figure legend, the reader is referred to the web version of this article).

standardised procedures [44,45]. SAXS data analysis was performed using McSAS, a Monte Carlo fitting programme that utilises a form-free, minimum assumption methodology [46].

3. Results and discussion

3.1. Ex-situ characterization

The acidity of the samples was studied with NH_3 adsorption at 100 °C followed by NH_3-TPD (Fig. 1). The number of acid sites was proportional to the amount of desorbed NH_3, and the desorption temperature reflected the acid strength of the catalyst. The NH_3 desorption in the lower temperature region, around 200 °C, was ascribed to weakly adsorbed NH_3, for instance, on weak Lewis acid sites or physisorbed NH_3 [47–52]. The peaks at approx. 273−285 °C were assigned to Lewis acid sites of PdO [26,52,53]. Additional peaks at 339 °C for the PdB40 sample and at 420 °C for the PdS43 sample were assigned to the strong Brønsted acid sites of the zeolite framework, as reported in the literature for H-beta and H-SSZ-13 zeolites [35,47,54,55]. The use of different zeolite supports resulted in distinctly different NH_3-TPD profiles. The highest acidity was exhibited by the PdB40 and PdS43 samples, with a total NH_3 desorption amount of 0.141 and 0.134 mmol per monolith, respectively. However, the acid strength and amount of strong acid sites of the PdB40 and PdS43 were different. Despite similar SAR, the PdS43 sample exhibited a higher number of strong Brønsted acid sites than the PdB40 sample, which was seen in the deconvolution of the NH_3-TPD (see Fig. S1). 77 % of the desorbed NH_3 of the PdS43 was released in the high temperature peak associated with Brønsted acid sites. The value for the PdB40 sample was 63 %. Our results are consistent with the work reported by Zheng et al. [35]. By contrast, the dealumination treatment of the PdB511 sample caused a loss in the total acid sites on the sample (the total amount of NH_3 desorption was 13-fold lower than that of the PdB40 sample) and eliminated the strong Brønsted acid sites, which was reflected by the absence of NH_3 desorption at temperatures above 300 °C.

Pd particle size was estimated with SAXS (Table 3, Figs. 2 and S2 (Supplementary material)) using samples that had been degreened, pretreated, and exposed to the experimental sequence used for operando XAS measurements at 360 °C (*i.e.* 30-min steady state CH_4 oxidation and 10 rich-lean pulse cycles). Note that the samples were subsequently cooled in 2 vol% O_2 to avoid any reduction of PdO. The results from SAXS were in good agreement with the STEM images in Fig. S3. However, the small PdO particles were difficult to distinguish in the STEM images, and consequently, the size of the small Pd particles was more accurately estimated with SAXS.

The PdB511 sample with the lowest Al content showed a broad range of Pd particle sizes with an average radius of 9 nm (Fig. 2a, Table 3). The formation of relatively large Pd particles in the PdB511 sample is not surprising as the interactions between the PdO and the B511 zeolite were expected to be weak due to the low acidity of this zeolite (Fig. 1). The strong acidity of zeolite frameworks with high Al content allows for the stabilization of well-dispersed PdO particles and/or monodispersed
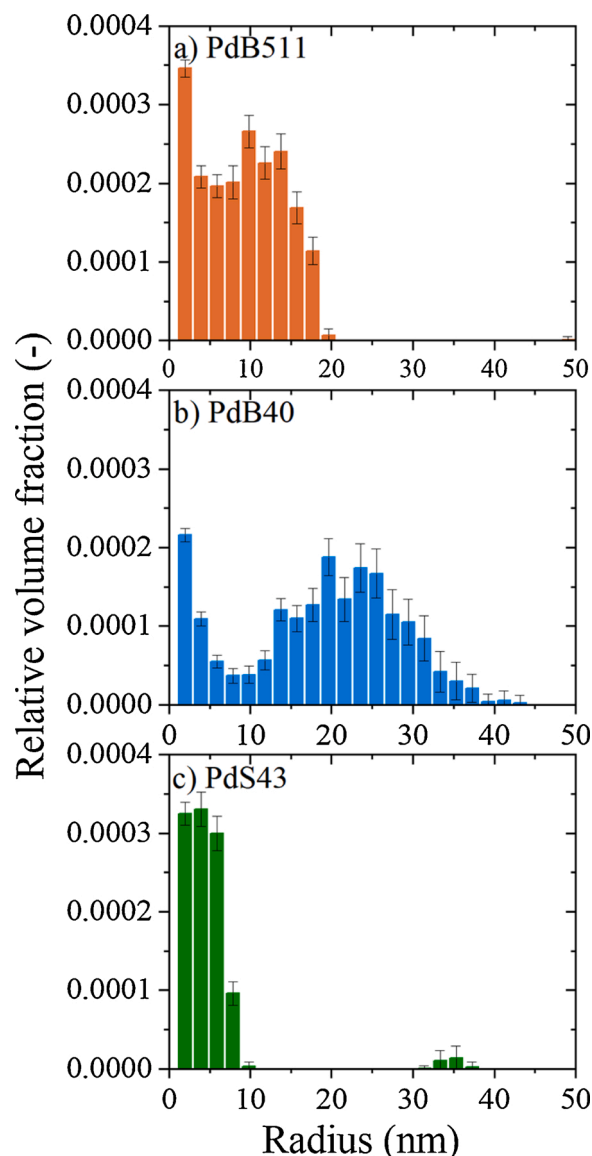
Table 3
Pd particle radius measured with Small-Angle X-ray Scattering (SAXS) and portion of Pd exchangeable with Na^+ obtained from NaCl titration. The full particle size distribution is shown in Fig. 2. The measurements were performed on the sample powder after rich-lean cycling at 360 °C and cooling to room temperature in the presence of O_2.

	Total average radius (nm)	Average radius of particles <10 nm (nm)	Average radius of particles >10 nm (nm)	Portion of Pd exchangeable with Na^+ (%)
PdB511	9.38 ± 0.54	5.39 ± 0.07	13.99 ± 0.09	4
PdB40	18.39 ± 0.20	3.76 ± 0.10	22.65 ± 0.21	13
PdS43	4.99 ± 0.57	4.24 ± 0.04	27.19 ± 14.12	2

Fig. 2. Pd particle size distribution of a) PdB511, b) PdB40, and c) PdS43 samples measured with Small-Angle X-ray Scattering (SAXS). The measurements were performed after rich-lean cycling at 360 °C and cooling to room temperature in the presence of O_2.

Pd ions [24,26,29,30,34,56]. Another factor that may also have contributed to the formation of large Pd particles in the PdB511 sample is the combination of the high hydrophobicity of the B511 zeolite with the incipient wetness method used to deposit Pd onto the zeolite. In a recent publication, Khivantsev et al. [57] have associated the formation of large Pd particles in zeolites with high SAR to the incomplete impregnation of the hydrophobic pores of the zeolites with the aqueous Pd solution.

The H-SSZ-13 zeolite in the PdS43 sample was able to stabilize the smallest PdO particles, on average with a radius of 5 nm, and a few large PdO clusters (Fig. 2c, Table 3). This is likely a result of strong PdO-zeolite interactions attributed to the high acidity of the S43 zeolite (Fig. 1) [24,26,29,30,34,56]. The PdB40 sample (Fig. 2b, Table 3) was dominated by large PdO particles (average radius 23 nm) in addition to a lower number of small particles (4 nm), although the SAR for the PdB40 sample was approximately the same as for the PdS43.

The amount of ion-exchanged Pd^{2+} in the zeolite-supported samples was estimated with NaCl titration, a method introduced by Ogura et al. [41] and utilized in several studies [35,37,58,59]. The results in Table 3

show that the PdB511 and PdS43 samples contained no or very little Na^+-exchangeable Pd, whereas about 10 % of the Pd in the PdB40 sample was removed from it in the NaCl solution. This means that the PdB40 sample contained the most monodispersed Pd ions. It has previously been reported that the formation of ion-exchanged Pd^{2+} is more difficult in H-SSZ-13 than in H-beta and H-ZSM-5 [35,38]. For instance, the formation of monodispersed Pd ions has been observed after oxidation at 750 °C in Pd/H-ZSM-5 [37,38] but not, or to a lesser extent, in Pd/H-SSZ-13 [36,38]. However, aging at 750 °C in the presence of water vapour has been found to result in the formation of monodispersed Pd in Pd/H-SSZ-13 [36,38]. This implies that both high temperatures and the presence of water vapour are required for the formation of monodispersed Pd ions in the PdS43 sample. As such conditions were not used in our study (maximum temperature of treatment 550 °C), the Pd remained as particles. Zheng et al. [35] have compared Pd supported on H-beta with H-SSZ-13 zeolites with similar SAR and found that a high portion of the Pd was ion-exchanged in the beta zeolite, whereas the formation of Pd particles was favoured for zeolite SSZ-13. The suggested reason for the difficulties in forming ion-exchanged Pd^{2+} in H-SSZ-13 compared to zeolites, such as H-beta and H-ZSM-5, is that the small pore size of SSZ-13 limits Pd diffusion, thus making Pd less mobile and less prone to rearrange into ion-exchanged Pd^{2+} species [35,38]. By contrast, the larger pore opening of beta and ZSM-5 zeolites is suggested to facilitate Pd mobility and consequently the formation of ion-exchanged Pd^{2+}. This may explain why Pd^{2+} ions were found in the PdB40 sample but not in the PdS43. The lack of Brønsted acid sites is the most obvious reason for the negligible amount of exchanged Pd^{2+} in the PdB511 sample. However, this does not explain the high number of large particles in the PdB40 sample with an average radius of about 22 nm, which was not present to the same extent in the PdB511 sample despite the same zeolite structure. Therefore, we suggest that the combination of large pore size and relatively high Al content caused the formation of large Pd particles together with monodispersed Pd ions.

3.2. Steady state CH4 oxidation

Steady state of CH_4 oxidation was tested at constant temperatures in a CH_4/O_2 feed for 30 min. The samples were degreened and pre-treated prior to this procedure (Table 2). The obtained CH_4 conversion at 360 °C is shown in Fig. 3. Both the PdB511 and PdS43 samples exhibited a similarly high level of CH_4 conversion. PdB40 was the least active sample with considerably less activity. This trend applied to all investigated temperatures (270−360 °C), however, the lower temperature was naturally accompanied by lower activity for all samples (Fig. S4).
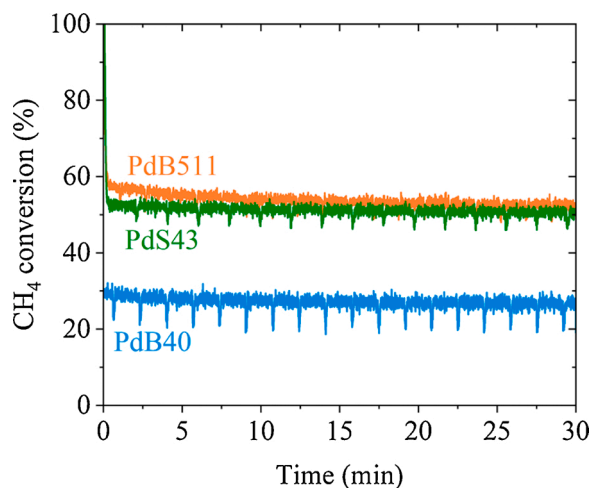

Fig. 3. Methane conversion at 360 °C for 30 min in 1000 ppm CH_4/2 vol% O_2 using degreened and pre-treated samples.
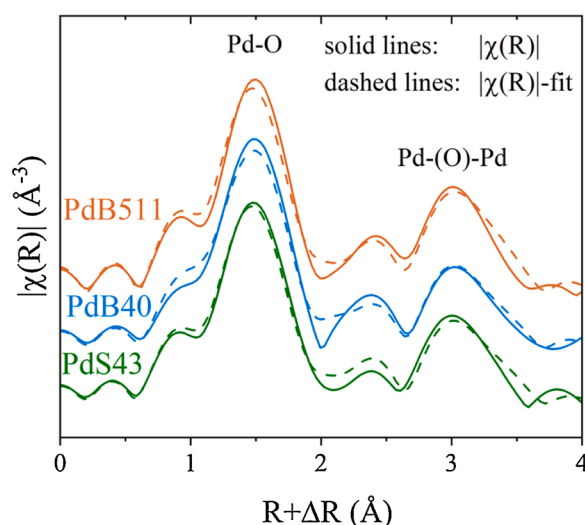

Fig. 4. Fourier transformed EXAFS spectra (non-phase shift corrected) recorded after 30 min of isothermal CH_4 oxidation at 360 °C (corresponding to the last minute in Fig. 3). Dashed lines represent EXAFS fits.

XANES spectra were collected after 30 min of isothermal CH_4 oxidation. The LCF of the PdO and Pd° references for the XANES spectra showed that all the samples had been fully oxidized after 30 min of isothermal CH_4 oxidation (Fig. S5). In other words, the samples exhibited significantly different levels of activity despite that all samples were fully oxidized. This means that the level of CH_4 oxidation was not exclusively related to the oxidation state of the Pd but was also influenced by other factors.

To obtain more insight into this behaviour, the EXAFS spectra corresponding to the last minute of the time-on-stream shown in Fig. 3 were analysed. The Fourier transformed k^2-weighted EXAFS spectra shown in Fig. 4 correspond to the average of all spectra collected during the last minute of the 30-min sequence shown in Fig. 3. All fitting results are given in Figs. S6, S7, and Table S1. The best fit of the FT-EXAFS spectra showed that the coordination environment of the Pd-O scattering shell at 1.5 Å (all values non-phase shift corrected) was complete ($CN_{Pd-O} \approx 4$, Table 4) for all samples, which was expected for oxidized samples. Another feature was present at 3.0 Å, which corresponded to the Pd-(O)-Pd scattering path. The coordination number of this path ($CN_{Pd-(o)-Pd}$) strongly correlated particle to PdO particle size. However, EXAFS is a bulk technique, meaning that the recorded spectra represent the average coordination environment of the absorbing Pd atom. Thus, a relatively low $CN_{Pd-(o)-Pd}$ value can either indicate small PdO particles or a few large PdO particles combined with a high number of isolated Pd entities without neighbouring Pd atoms [36–38]. Based on the EXAFS analysis, $CN_{Pd-(o)-Pd}$ decreased in the order of PdB511 ($CN_{Pd-(o)-Pd} = 10.1$, 360 °C) > PdS43 ($CN_{Pd-(o)-Pd} = 8.4$, 360 °C) ≈ PdB40 ($CN_{Pd-(o)-Pd} = 8.1$, 360 °C) as shown in Table 4. The trend was the same for all investigated temperatures (Table S1). This is in reasonable agreement with the aforementioned results of the characterization of Pd species from the SAXS and STEM techniques. The fact that the Pd-(O)-Pd shell of the PdB40 sample was not fully coordinated ($CN_{Pd-(o)-Pd} < 12$) is likely because the PdB40 sample also contained monodispersed Pd ions without neighbouring Pd atoms, which lowered the average $CN_{Pd-(o)-Pd}$. The monodispersed Pd ions without neighbouring Pd atoms were also found in the NaCl titration (Table 3) results.

3.3. CH4 oxidation under alternating rich and lean pulses

The catalyst samples were further evaluated under repeated rich (CH_4/Ar) and lean ($CH_4/O_2/Ar$) pulses. The rich-lean sequences were repeated ten times to ensure stable performance, which can be seen by

Table 4

Parameters from fitting the EXAFS spectra in Fig. 4, recorded at 360 °C after 30 min of CH_4 oxidation (prior to the first rich pulse). All parameters are given in Table S1. The estimated uncertainty for fitted CN is about ± 10 % and ±0.02 Å for R.

Temperature (°C)	Scattering Path	σ^2 (Å²)*10⁵	R (Å)	CN		
				PdB511	PdB40	PdS43
360	Pd-O	640	2.008	4.2	4.1	4.0
	Pd-Pd	1452	2.728	0.0	0.1	0.0
	Pd(-O-)Pd.1	1091	3.044	3.4	2.7	2.8
	Pd(-O-)Pd.2		3.433	6.7	5.4	5.6
330	Pd-O	600	2.009	3.6	3.8	3.9
	Pd-Pd	1385	2.728	1.2	0.2	0.0
	Pd(-O-)Pd.1	978	3.044	2.7	2.7	3.0
	Pd(-O-)Pd.2		3.434	5.3	5.4	6.0
300	Pd-O	550	2.011	4.0	3.7	3.9
	Pd-Pd	1317	2.728	0.0	0.4	0.0
	Pd(-O-)Pd.1	903	3.035	3.1	2.7	2.7
	Pd(-O-)Pd.2		3.424	6.3	5.4	5.4
270	Pd-O	490	2.014	3.7	4.0	4.0
	Pd-Pd	1250	2.728	0.9	0.0	0.0
	Pd(-O-)Pd.1	784	3.038	2.6	2.7	2.3
	Pd(-O-)Pd.2		3.427	5.2	5.4	4.6

the nearly identical Pd^{2+} profiles and CH_4 oxidation activity during cycle 9-10 in Figs. S8 and S9. The focus of the following analysis will therefore only concern the last two sequences (cycle 9-10), shown in Fig. 5.

3.3.1. Response to rich pulses

The rich pulses at 360 °C and 330 °C (Fig. 5a-b) resulted in nearly full reduction of all the samples (remaining oxidized fraction approx. 10 % Pd^{2+}). The extent of reduction was lower (Fig. 5c-d) at lower temperatures. The PdB40 sample could not be reduced at 300 °C (Fig. 5c) and remained nearly completely oxidized throughout the rich pulses. The PdB511 (approx. 20 % Pd^{2+}) and PdS43 (approx. 30 % Pd^{2+}) samples reduced easier at this temperature. The PdB40 and PdS43 samples retained the oxide form (almost 100 % Pd^{2+}) at a lower temperature (270 °C, Fig. 5d), whereas the PdB511 sample was partially reduced (approx. 70 % Pd^{2+}). The responses to the rich pulses revealed that the samples had major differences in their inherent resistance to reduction. The order of reduction was PdB511> PdS43> PdB40, suggesting that both the SAR and the type of zeolite framework strongly influence the stability of Pd^{2+}. The above characterization with NaCl titration

indicated that the PdB40 sample contained ion-exchanged Pd^{2+} at the end of the lean pulse. However, it is not clear whether the mono-dispersed Pd ions remained in the same state during the rich pulse. Previous studies have shown that monoatomic Pd^{2+} species and small PdO particles rearrange into Pd particles under rich conditions [29–32, 35]. It is possible that the monodispersed Pd ions in the PdB40 sample contributed to the stability of Pd against reduction (Fig. 5c-d).

The EXAFS data (Fig. 6) of the samples reduced under rich pulses at 360 °C and 330 °C were characterized by an intense Pd-Pd shell of metallic Pd° at 2.5 Å (non-phase shift corrected). Fitting this shell yielded $CN_{Pd-Pd} \approx 10$ for all samples. Large Pd° particles in about the same size range formed in all samples. Assuming spherical fcc Pd° particles with a density of 12.02 g/cm³, the calculated particle diameter based on Hill's function [60] was 2.3 nm for $CN_{Pd-Pd} = 10$. CN_{Pd-Pd} may be slightly underestimated but shows that the particles were located on the external zeolite surfaces. Fitting fully oxidized PdB40 (270−300 °C) and PdS43 (270 °C) samples returned $CN_{Pd-O} \approx 4$ and $CN_{Pd-(O)-Pd} \approx 7$, indicating that well-dispersed PdO particles and/or large PdO particles in combination with ion-exchanged Pd^{2+} were present in the samples. Based on the ex-situ characterization of the oxidized samples, it is likely
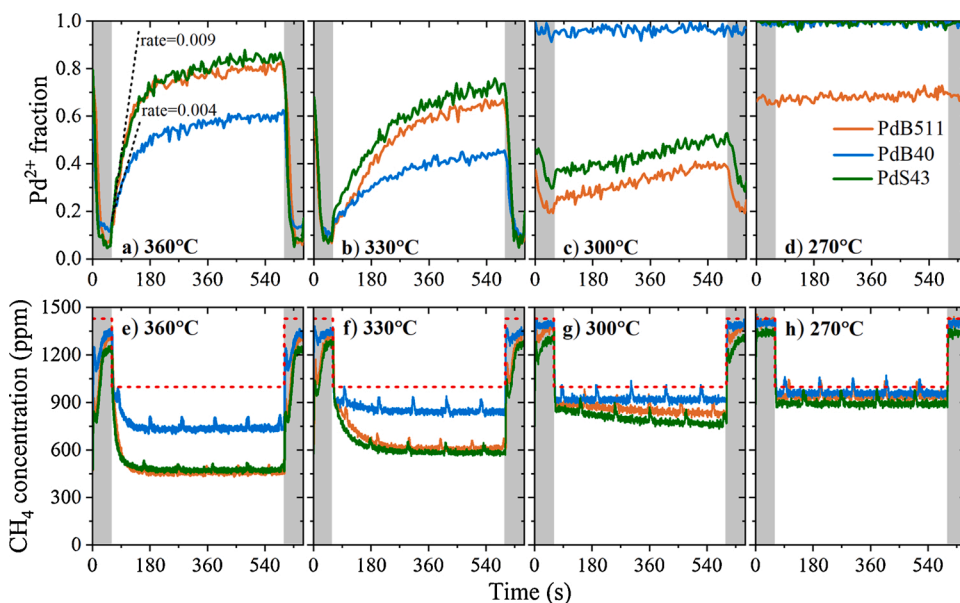

Fig. 5. Data acquired during the 9th rich-lean sequence and the 10th rich pulse at the indicated temperatures. (a-d) Fraction of Pd^{2+} obtained from LCF of XANES spectra. (e-h) Corresponding outlet concentration of CH_4. The red dashed line illustrates the inlet CH_4 concentration. The oxidation rate (ΔPd^{2+} fraction/Δt, s⁻¹) at the beginning of the lean pulse is indicated in (a). Grey and white areas represent rich and lean pulses, respectively. (For interpretation of the references to colour in this figure legend, the reader is referred to the web version of this article).
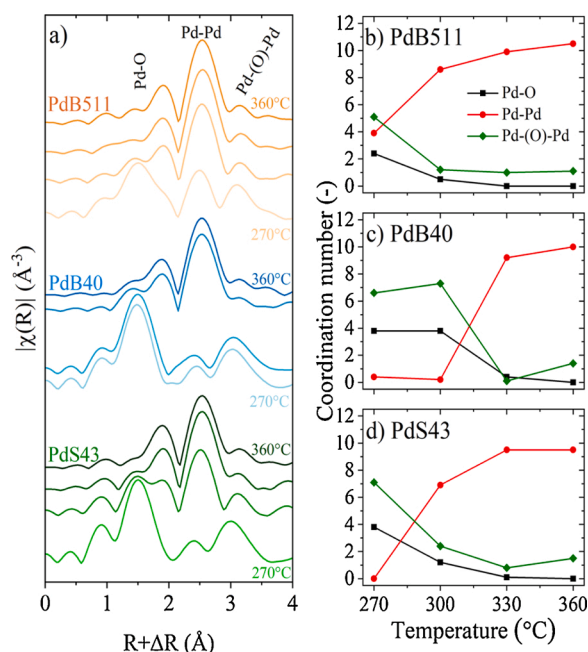
Fig. 6. Data retrieved from the extended X-ray absorption fine structure (EXAFS) spectra measured at the end of the rich pulses shown in Fig. 5. a) Fourier transformed EXAFS spectra (non-phase shift corrected) at 360, 330, 300, and 270 °C. The coordination numbers (CN), determined on the basis of curve fitting of EXAFS spectra in a, are shown in b (PdB511), c (PdB40), and d (PdS43). Values for R and σ^2 are given in Table 4. All fitting parameters are shown in Tables S2–S5.

Fig. 7. Data retrieved from the extended X-ray absorption fine structure (EXAFS) spectra measured at the end of the lean pulse in Fig. 5. a) Fourier transformed EXAFS spectra (non-phase shift corrected) at 360, 330, 300, and 270 °C. b-d) Coordination number (CN) determined on the basis of curve fitting of EXAFS spectra for the PdB511, PdB40, and PdS43 samples. Values for R and σ^2 are given in Table 4. All fitting parameters are shown in Tables S2–S5.

that the PdB40 sample contained small PdO particles, monodispersed Pd ions, and large PdO particles, and the PdS43 sample probably contained mainly well-dispersed PdO particles.

3.3.2. Response to lean pulses

The introduction of oxygen was accompanied by the re-oxidation of Pd. The PdB511 and PdS43 samples displayed close to identical re-oxidation profiles at 360 °C (Fig. 5a) and had the highest Pd^{2+} fraction (approx. 83 % Pd^{2+}) at the end of the first lean pulse. These samples had the fastest oxidation rate at the beginning of the lean pulse. The average oxidation rate (ΔPd^{2+} fraction/Δt) during the first 30 s of the lean pulse at 360 °C was 0.009 s^{-1} for the PdB511 and PdS43 samples, whereas it was only 0.004 s^{-1} for the PdB40. The PdB40 sample was the most difficult one to re-oxidize (approx. 59 % Pd^{2+}). The same trend was observed at 330 °C (Fig. 5b), *i.e.* the PdS43 and PdB511 samples were the easiest to re-oxidize, followed by the PdB40. This order was maintained at 300 °C (Fig. 5c), except for the PdB40 sample, which remained completely oxidized, as 300 °C is below its critical reduction temperature. The PdB40 and PdS43 samples remained completely oxidized at 270 °C, whereas the PdB511 sample maintained approx. 70 % Pd^{2+} constantly (Fig. 5d).

The EXAFS spectra in Fig. 7 were acquired at the end of the 10th lean pulse at 360, 330, 300, and 270 °C. The samples were characterized by a metallic Pd-Pd peak in addition to the Pd-O and Pd-(O)-Pd peaks in the partially oxidized state of the samples. The Pd-Pd peak probably represents Pd° cores of large partly oxidized Pd particles. The Pd-O and the Pd-(O)-Pd shells of the EXAFS probably represent PdO particles and the PdO outer shells of large particles. The PdB40 sample also had isolated Pd^{2+} species. The PdB40 sample did not reduce at 300 °C and 270 °C, and the PdS43 sample did not reduce at 270 °C.

Therefore, the EXAFS spectra recorded during the rich and lean pulses appear similar (Figs. 6 and 7).
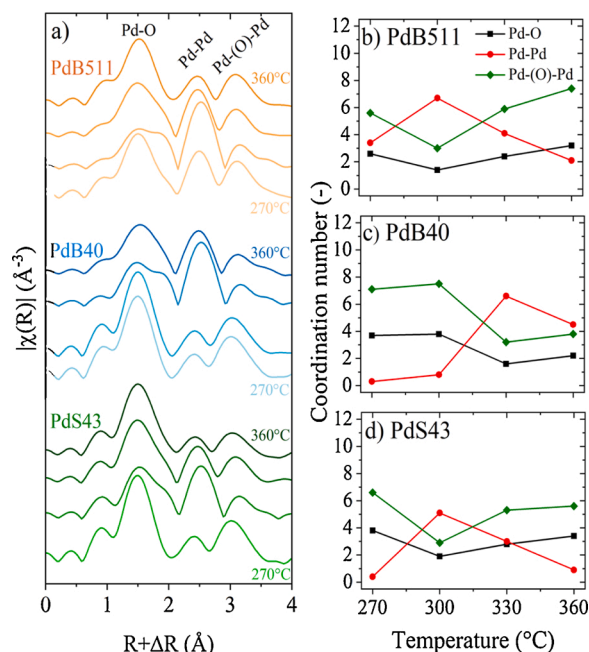
3.3.3. CH_4 oxidation activity under alternated rich and lean pulses

Fig. 5e–h shows the measured outlet concentrations of CH_4 during the rich-lean pulse experiments. A comparison of the CH_4 outlet concentration (Fig. 5e–h) and the Pd^{2+} fraction (Fig. 5a–d) recorded during exposure to rich and lean pulses shows that the CH_4 conversion can be directly related to the oxidation state of Pd. In other words, CH_4 oxidation increased when the Pd was being oxidized [5–7]. However, the CH_4 conversion was approximately the same for the completely oxidized catalysts prior to the first rich pulse (Fig. 3) and at the end of the lean pulse (Fig. 5e–h), where the catalysts had only been partially oxidized. This means that the same activity levels were obtained despite the different oxidation states. It has previously been reported that the CH_4 oxidation activity only increases up to a certain level of PdO formation, and that further oxidation of the Pd particles does not influence the catalytic activity of CH_4 oxidation [7,12], which is in line with our results.

The PdB511 and PdS43 samples yielded about the same level of CH_4 conversion and showed about the same state of oxidation throughout the pulse experiments. By contrast, the PdB40 sample, which was the most difficult sample to reduce and re-oxidize, had the lowest level of CH_4 conversion. Approximately 10 % of the Pd in the PdB40 sample is estimated to have been ion-exchanged with the Brønsted acid sites in the zeolite at the end of the lean pulse at 360 °C, and large Pd particles were found using SAXS and STEM. This combination of large Pd particles and monodispersed Pd ions appears to have had a detrimental effect on the reduction and re-oxidization of Pd, and on the activity of the PdB40 sample. Previous studies have found that monodispersed Pd ions are not active or are less active than Pd particles [24,26,32,33]. One possible explanation for the lower activity of the PdB40 sample is that the combination of ion-exchanged Pd^{2+} and large PdO particles resulted in a lower number of catalytically active PdO sites. It has been reported that CH_4 oxidation may have a volcano-shaped dependence on Pd particle size [61,62], but a linear increase has also been observed [63]. The reason for the differences is the strength of the metal support interaction: strong metal-support interaction in Pd/γ-Al$_2$O$_3$ gives a linear

increase, whereas a volcano-shaped correlation was found for weak interactions in Pd/MgO [63]. To gain further information regarding the effect Pd-particle sizes, the turnover frequencies (TOFs) were calculated at 270 °C where the CH$_4$ conversion over the three catalysts was low (4, 7, and 12.5 % for PdB40, PdB511, and PdS43, respectively), and differential reactor conditions can be applied. The TOF monotonously increased from 0.017 to 0.027 s^{-1} as the particle size increased from 5.0–18.4 nm, as shown in Fig. S10. Thus, in term of the TOF, the larger the PdO particles, the larger CH$_4$ oxidation rate. This dependence of TOF on particle size suggests that there were strong metal-support interactions. It should be noted that because the Pd dispersion obtained from SAXS is used in the TOF calculations, the TOF is per active Pd site. However, many of the Pd sites are not accessible in the case of large particles, thus accounting for a low overall conversion.

Another possible explanation for the lower activity found for the PdB40 sample is related to the fact that complete CH$_4$ oxidation over PdO is considered to occur *via* the Mars van Krevelen mechanism [4,64, 65], *i.e.* CH$_4$ molecules react with oxygen atoms of the PdO to form CO$_2$ and H$_2$O. Thus, the CH$_4$ oxidation reaction should benefit from a catalyst that easily forms catalytically active PdO. However, if the interactions between Pd and O are very strong, *i.e.* if the PdO is difficult to reduce, the CH$_4$ oxidation rate may decrease [4,20]. Consequently, CH$_4$ oxidation benefits from a catalyst with rapid transitions between oxidized and reduced states upon switching between lean and rich conditions. Since those rapid transitions between oxidized and reduced state were found for PdS43 and PdB511, but not for PdB40, our interpretation may explain why the CH$_4$ conversion level generally decreased in the order, PdS43 ≈ PdB511 > PdB40.

Lower sample temperature resulted in lower activity and less efficient reduction and re-oxidation. 270 °C and 300 °C were not sufficiently high temperatures to reduce PdB40, as shown in Fig. 5c-d, so Pd in PdB40 remained completely oxidized. This was reflected by the absence of CH$_4$ conversion for the PdB40 sample in Fig. 5g-h. 300 °C was not high enough to activate the C–H bond, which is required to initiate the PdO reduction by CH$_4$ and the catalysed CH$_4$ oxidation reaction [14]. The PdS43 sample exhibited the same behaviour at 270 °C. The PdB511 and PdS43 samples had only been partly reduced and re-oxidized at 300 °C, which was also reflected by the correspondingly low CH$_4$ conversion on these catalysts at 300 °C.

The formation of well-dispersed Pd particles in the PdS43 sample explains the facilitated reduction and re-oxidation of Pd, and the high level of activity for CH$_4$ oxidation shown in Fig. 5. It is, however, possible that the particles present in the PdB511 sample were small enough to provide the same effect, as the performance of the PdB511 sample was similar to that of the PdS43. By contrast, the coexistence of large Pd particles and monodispersed Pd ions in the PdB40 sample hampered Pd reduction and re-oxidation, thus providing a low level of CH$_4$ oxidation. This agrees with our previous findings [17,24,25], *i.e.* Pd/zeolites with dispersed and stabilized Pd particles have a higher CH$_4$ oxidation, impeded by Pd sintering and the formation of ion-exchanged Pd^{2+} species. It was demonstrated that Pd particles were stabilized by the formation of mesopores in the zeolite through mild desilication, the removal of extra framework alumina by selective dealumination [25], and the removal of acid sites in the zeolite either by full ion-exchange with alkali metals [17,25] or by using highly siliceous zeolites [24]. It should be noted that the zeolite pores of beta and SSZ-13 are much smaller (<1 nm [66]) than the particles observed with the characterization methods used in the present study. This suggests that the particles were located mainly on external zeolite surfaces or possibly within the mesopores of the zeolite. We suggest that the selection of the zeolite support is crucial in order to obtain highly active CH$_4$ oxidation catalysts. The selection should take into consideration the necessity to minimize the formation of monodispersed Pd atoms and to promote good dispersion of Pd particles simultaneously.

4. Conclusions

The effect of different zeolite supports for Pd-based CH$_4$ oxidation catalysts using activity tests and various characterization techniques was examined using three different zeolite supports, H-beta (SAR = 511 and 40) and H-SSZ-13 (SAR = 43). The results clearly show that both the type of zeolite framework and the SAR impact the type of Pd species formed, as well as the catalytic performance. Our findings suggest that the selection of a zeolite support is paramount to minimizing the formation of ion-exchanged Pd^{2+} species and the formation of well-dispersed Pd particles in order to obtain a highly active CH$_4$ oxidation catalyst. The formation of ion-exchanged Pd^{2+} and large Pd particles can be prevented by using highly siliceous zeolites with a low number of Brønsted acidic sites and small-pore zeolites, which decrease Pd mobility. By contrast, large pore size and low SAR facilitate the formation of ion-exchanged Pd^{2+} species and large Pd particles. This makes the catalyst more difficult to reduce and to re-oxidize and is accompanied by a low conversion of CH$_4$. The catalyst with the highest conversion of CH$_4$ was characterized by rapid transitions between metallic and oxidized Pd during switches between rich and lean pulses.

CRediT authorship contribution statement

Ida Friberg: Investigation, Formal analysis, Conceptualization, Writing - original draft. **Adam H. Clark:** Investigation, Formal analysis, Writing - review & editing. **Phuoc Hoang Ho:** Formal analysis, Writing - review & editing. **Nadezda Sadokhina:** Investigation, Supervision, Writing - review & editing. **Glen J. Smales:** Investigation, Formal analysis, Writing - review & editing. **Jungwon Woo:** Investigation, Writing - review & editing. **Xavier Auvray:** Investigation, Writing - review & editing. **Davide Ferri:** Supervision, Conceptualization, Methodology, Writing - review & editing. **Maarten Nachtegaal:** Supervision, Conceptualization, Methodology, Writing - review & editing. **Oliver Kröcher:** Supervision, Conceptualization, Methodology, Writing - review & editing. **Louise Olsson:** Supervision, Conceptualization, Methodology, Writing - review & editing.

Declaration of Competing Interest

The authors declare that they have no known competing financial interests or personal relationships that could have appeared to influence the work reported in this paper.

Appendix A. Supplementary data

Supplementary material related to this article can be found, in the online version, at doi:https://doi.org/10.1016/j.cattod.2020.11.026.

References

[1] IPCC, Climate Change 2014: Synthesis Report, Geneva, Switzerland, 2014, 2014.

[2] R. Gholami, M. Alyani, K.J. Smith, Deactivation of Pd catalysts by water during low temperature methane oxidation relevant to natural gas vehicle converters, Catalysts 5 (2015) 561–594.

[3] Y.-H. Chin, C. Buda, M. Neurock, E. Iglesia, Consequences of metal–oxide interconversion for C–H bond activation during CH$_4$ reactions on Pd catalysts, J. Am. Chem. Soc. 135 (2013) 15425–15442.

[4] K. Fujimoto, F.H. Ribeiro, M. Avalos-Borja, E. Iglesia, Structure and reactivity of PdO$_x$/ZrO$_2$, catalysts for methane oxidation at low temperatures, J. Catal. 179 (1998) 431–442.

[5] J.G. McCarty, Kinetics of PdO combustion catalysis, Catal. Today 26 (1995) 283–293.

[6] R.J. Farrauto, M.C. Hobson, T. Kennelly, E.M. Waterman, Catalytic chemistry of supported palladium for combustion of methane, Appl. Catal. A: Gen. 81 (1992) 227–237.

[7] R. Burch, F.J. Urbano, Investigation of the active state of supported palladium catalysts in the combustion of methane, Appl. Catal. A: Gen. 124 (1995) 121–138.

[8] M. Lyubovsky, L. Pfefferle, Methane combustion over the alpha-alumina supported Pd catalyst: Activity of the mixed Pd/PdO state, Appl. Catal. A: Gen. 173 (1998) 107–119.

[9] N.M. Kinnunen, J.T. Hirvi, T. Venalainen, M. Suvanto, T.A. Pakkanen, Procedure to tailor activity of methane combustion catalyst: Relation between Pd/PdOx active sites and methane oxidation activity, Appl. Catal. A: Gen. 397 (2011) 54–61.

[10] P.O. Thevenin, E. Pocoroba, L.J. Pettersson, H. Karhu, I.J. Vayrynen, S.G. Jaras, Characterization and activity of supported palladium combustion catalysts, J. Catal. 207 (2002) 139–149.

[11] J. Nilsson, P.A. Carlsson, S. Fouladvand, N.M. Martin, J. Gustafson, M.A. Newton, E. Lundgren, H. Gronbeck, M. Skoglundh, Chemistry of supported palladium nanoparticles during methane oxidation, ASC Catal. 5 (2015) 2481–2489.

[12] J.N. Carstens, S.C. Su, A.T. Bell, Factors affecting the catalytic activity of Pd/ZrO$_2$ for the combustion of methane, J. Catal. 176 (1998) 136–142.

[13] K. Murata, D. Kosuge, J. Ohyama, Y. Mahara, S. Yamamoto, S. Arai, A. Satsuma, Exploiting metal–support interactions to tune the redox properties of supported Pd catalysts for methane combustion, ASC Catal. 10 (2020) 1381–1387.

[14] Y.H. Chin, E. Garcia-Dieguez, E. Iglesia, Dynamics and thermodynamics of Pd-PdO phase transitions: Effects of Pd cluster size and kinetic implications for catalytic methane combustion, J. Phys. Chem. C 120 (2016) 1446–1460.

[15] R. Burch, M.J. Hayes, C-H bond activation in hydrocarbon oxidation on solid catalysts, J. Mol. Catal. A: Chem. 100 (1995) 13–33.

[16] N.M. Martin, J. Nilsson, M. Skoglundh, E.C. Adams, X. Wang, P. Velin, G. Smedler, A. Raj, D. Thompsett, H.H. Brongersma, T. Grehl, G. Agostini, O. Mathon, S. Carlson, K. Norén, F.J. Martinez-Casado, Z. Matej, O. Balmes, P.-A. Carlsson, Characterization of surface structure and oxidation/reduction behavior of Pd–Pt/Al$_2$O$_3$ model catalysts, J. Phys. Chem. C 120 (2016) 28009–28020.

[17] A.W. Petrov, D. Ferri, F. Krumeich, M. Nachtegaal, J.A. van Bokhoven, O. Kröcher, Stable complete methane oxidation over palladium based zeolite catalysts, Nat. Commun. 9 (2018) 2545.

[18] H. Yoshida, T. Nakajima, Y. Yazawa, T. Hattori, Support effect on methane combustion over palladium catalysts, Appl. Catal. B: Environ. 71 (2007) 70–79.

[19] Y. Yazawa, H. Yoshida, N. Takagi, S. Komai, A. Satsuma, T. Hattori, Acid strength of support materials as a factor controlling oxidation state of palladium catalyst for propane combustion, J. Catal. 187 (1999) 15–23.

[20] R.F. Hicks, H.H. Qi, M.L. Young, R.G. Lee, Structure sensitivity of methane oxidation over platinum and palladium, J. Catal. 122 (1990) 280–294.

[21] H. Stotz, L. Maier, A. Boubnov, A.T. Gremminger, J.D. Grunwaldt, O. Deutschmann, Surface reaction kinetics of methane oxidation over PdO, J. Catal. 370 (2019) 152–175.

[22] I. Czekaj, K.A. Kacprzak, J. Mantzaras, CH$_4$ combustion cycles at Pd/Al$_2$O$_3$ – important role of support and oxygen access, Phys. Chem. Chem. Phys. 15 (2013) 11368–11374.

[23] S. Colussi, A. Trovarelli, C. Cristiani, L. Lietti, G. Groppi, The influence of ceria and other rare earth promoters on palladium-based methane combustion catalysts, Catal. Today 180 (2012) 124–130.

[24] I. Friberg, N. Sadokhina, L. Olsson, The effect of Si/Al ratio of zeolite supported Pd for complete CH$_4$ oxidation in the presence of water vapor and SO$_2$, Appl. Catal. B: Environ. 250 (2019) 117–131.

[25] A.W. Petrov, D. Ferri, O. Kröcher, J.A. van Bokhoven, Design of stable palladium-based zeolite catalysts for complete methane oxidation by postsynthesis zeolite modification, ASC Catal. 9 (2019) 2303–2312.

[26] K. Okumura, E. Shinohara, M. Niwa, Pd loaded on high silica beta support active for the total oxidation of diluted methane in the presence of water vapor, Catal. Today 117 (2006) 577–583.

[27] J.B. Lim, D. Jo, S.B. Hong, Palladium-exchanged small-pore zeolites with different cage systems as methane combustion catalysts, Appl. Catal. B: Environ. 219 (2017) 155–162.

[28] Y. Zhang, P. Glarborg, K. Johansen, M.P. Andersson, T.K. Torp, A.D. Jensen, J.M. Christensen, A rhodium-based methane oxidation catalyst with high tolerance to H$_2$O and SO$_2$, ACS Catal. 10 (2020) 1821–1827.

[29] K. Okumura, M. Niwa, Control of the dispersion of Pd through the interaction with acid sites of zeolite studied by EXAFS, Top. Catal. 18 (2002) 85–89.

[30] K. Okumura, M. Niwa, Regulation of the dispersion of PdO through the interaction with acid sites of zeolite studied by extended X-ray absorption fine structure, J. Phys. Chem. B 104 (2000) 9670–9675.

[31] K. Okumura, R. Yoshimoto, T. Uruga, H. Tanida, K. Kato, S. Yokota, M. Niwa, Energy-dispersive XAFS studies on the spontaneous dispersion of PdO and the formation of stable Pd clusters in zeolites, J. Phys. Chem. B 108 (2004) 6250–6255.

[32] A. Ali, W. Alvarez, C.J. Loughran, D.E. Resasco, State of Pd on H-ZSM-5 and other acidic supports during the selective reduction of NO by CH$_4$ studied by EXAFS/XANES, Appl. Catal. B: Environ. 14 (1997) 13–22.

[33] I. Friberg, A. Wang, L. Olsson, Hydrothermal aging of Pd/LTA monolithic catalyst for complete CH$_4$ oxidation, Catalysts 10 (2020) 517.

[34] O. Mihai, L. Trandafilovic, T. Wentworth, F.F. Torres, L. Olsson, The effect of Si/Al ratio for Pd/BEA and Pd/SSZ-13 used as passive NO$_x$ adsorbers, Top. Catal. 61 (2018) 2007–2020.

[35] Y. Zheng, L. Kovarik, M.H. Engelhard, Y. Wang, Y. Wang, F. Gao, J. Szanyi, Low-temperature Pd/Zeolite passive NO$_x$ adsorbers: structure, performance, and adsorption chemistry, J. Phys. Chem. C 121 (2017) 15793–15803.

[36] Y. Ryou, J. Lee, S.J. Cho, H. Lee, C.H. Kim, D.H. Kim, Activation of Pd/SSZ-13 catalyst by hydrothermal aging treatment in passive NO adsorption performance at low temperature for cold start application, Appl. Catal. B: Environ. 212 (2017) 140–149.

[37] J. Lee, Y. Ryou, S.J. Cho, H. Lee, C.H. Kim, D.H. Kim, Investigation of the active sites and optimum Pd/Al of Pd/ZSM-5 passive NO adsorbers for the cold-start application: Evidence of isolated-Pd species obtained after a high-temperature thermal treatment, Appl. Catal. B: Environ. 226 (2018) 71–82.

[38] J. Lee, Y. Ryou, S. Hwang, Y. Kim, S.J. Cho, H. Lee, C.H. Kim, D.H. Kim, Comparative study of the mobility of Pd species in SSZ-13 and ZSM-5, and its implication for their activity as passive NO$_x$ adsorbers (PNAs) after hydro-thermal aging, Catal. Sci. Technol. 9 (2019) 163–173.

[39] O. Müller, M. Nachtegaal, J. Just, D. Lutzenkirchen-Hecht, R. Frahm, Quick-EXAFS setup at the SuperXAS beamline for in situ X-ray absorption spectroscopy with 10 ms time resolution, J. Synchrotron Rad. 23 (2016) 260–266.

[40] G.L. Chiarello, M. Nachtegaal, V. Marchionni, L. Quaroni, D. Ferri, Adding diffuse reflectance infrared Fourier transform spectroscopy capability to extended x-ray-absorption fine structure in a new cell to study solid catalysts in combination with a modulation approach, Rev. Sci. Instrum. 85 (2014) 074102.

[41] A.H. Clark, J. Imbao, R. Frahm, M. Nachtegaal, ProQEXAFS: a highly optimized parallelized rapid processing software for QEXAFS data, J. Synchrotron Rad. 27 (2020) 551–557.

[42] B. Ravel, M. Newville, ATHENA, ARTEMIS, HEPHAESTUS: data analysis for X-ray absorption spectroscopy using IFEFFIT, J. Synchrotron Rad. 12 (2005) 537–541.

[43] M. Ogura, M. Hayashi, S. Kage, M. Matsukata, E. Kikuchi, Determination of active palladium species in ZSM-5 zeolite for selective reduction of nitric oxide with methane, Appl. Catal. B: Environ. 23 (1999) 247–257.

[44] J. Filik, A.W. Ashton, P.C.Y. Chang, P.A. Chater, S.J. Day, M. Drakopoulos, M. W. Gerring, M.L. Hart, O.V. Magdysyuk, S. Michalik, A. Smith, C.C. Tang, N. J. Terrill, M.T. Wharmby, H. Wilhelm, Processing two-dimensional X-ray diffraction and small-angle scattering data in DAWN 2, J. Appl. Crystallogr. 50 (2017) 959–966.

[45] B.R. Pauw, A.J. Smith, T. Snow, N.J. Terrill, A.F. Thunemann, The modular small-angle X-ray scattering data correction sequence, J. Appl. Crystallogr. 50 (2017) 1800–1811.

[46] I. Bressler, B.R. Pauw, A.F. Thunemann, McSAS: software for the retrieval of model parameter distributions from scattering patterns, J. Appl. Crystallogr. 48 (2015) 962–969.

[47] D. Wang, Y. Jangjou, Y. Liu, M.K. Sharma, J.Y. Luo, J.H. Li, K. Kamasamudram, W. S. Epling, A comparison of hydrothermal aging effects on NH$_3$-SCR of NO$_x$ over Cu-SSZ-13 and Cu-SAPO-34 catalysts, Appl. Catal. B: Environ. 165 (2015) 438–445.

[48] S. Han, J. Cheng, C.K. Zheng, Q. Ye, S.Y. Cheng, T.F. Kang, H.X. Dai, Effect of Si/Al ratio on catalytic performance of hydrothermally aged Cu-SSZ-13 for the NH$_3$-SCR of NO in simulated diesel exhaust, Appl. Surf. Sci. 419 (2017) 382–392.

[49] A. Aranzabal, J.A. Gonzalez-Marcos, A. Romero-Saez, J.R. Gonzalez-Velasco, M. Guillemot, P. Magnoux, Stability of protonic zeolites in the catalytic oxidation of chlorinated VOCs (1,2-dichloroethane), Appl. Catal. B: Environ. 88 (2009) 533–541.

[50] R. Srivastava, N. Iwasa, S. Fujita, M. Arai, Dealumination of zeolite beta catalyst under controlled conditions for enhancing its activity in acylation and esterification, Catal. Lett. 130 (2009) 655–663.

[51] M.A. Arribas, F. Marquez, A. Martinez, Activity, selectivity, and sulfur resistance of Pt/WO$_x$-ZrO$_2$ and Pt/Beta catalysts for the simultaneous hydroisomerization of n-heptane and hydrogenation of benzene, J. Catal. 190 (2000) 309–319.

[52] Y. Lou, J. Ma, W.D. Hu, Q.G. Dai, L. Wang, W.C. Zhan, Y.L. Guo, X.M. Cao, Y. Guo, P. Hu, G.Z. Lu, Low-temperature methane combustion over Pd/H-ZSM-5: active Pd sites with specific electronic properties modulated by acidic sites of H-ZSM-5, ASC Catal. 6 (2016) 8127–8139.

[53] N.M. Kinnunen, J.T. Hirvi, T. Venäläinen, M. Suvanto, T.A. Pakkanen, Procedure to tailor activity of methane combustion catalyst: relation between Pd/PdOx active sites and methane oxidation activity, Appl. Catal. A: Gen. 397 (2011) 54–61.

[54] C. Li, K. Fujimoto, Synthesis gas conversion to isobutane-rich hydrocarbons over a hybrid catalyst containing Beta zeolite – role of doped palladium and influence of the SiO$_2$/Al$_2$O$_3$ ratio, Catal. Sci. Technol. 5 (2015) 4501–4510.

[55] D. Wang, F. Gao, C.H.F. Peden, J.H. Li, K. Kamasamudram, W.S. Epling, Selective catalytic reduction of NO$_x$ with NH$_3$ over a Cu-SSZ-13 catalyst prepared by a solid-state ion-exchange method, Chemcatchem 6 (2014) 1579–1583.

[56] K. Okumura, M. Niwa, Metal-support interaction which controls the oxidation state, structure and catalysis of Pd, Catal. Surv. Jpn. 5 (2002) 121–126.

[57] K. Khivantsev, N.R. Jaegers, L. Kovarik, J.C. Hanson, F. Tao, Y. Tang, X.Y. Zhang, I. Z. Koleva, H.A. Aleksandrov, G.N. Vayssilov, Y. Wang, F. Gao, J. Szanyi, Achieving atomic dispersion of highly loaded transition metals in small-pore zeolite SSZ-13: high-capacity and high-efficiency low-temperature CO and passive NO$_x$ adsorbers, Angew. Chem. Int. Ed. 57 (2018) 16672–16677.

[58] M. Jiang, J. Wang, J.Q. Wang, M.Q. Shen, The influence of Si/Al ratios on adsorption and desorption characterizations of Pd/beta served as cold-start catalysts, Materials 12 (2019) 14.

[59] B.B. Zhang, M.Q. Shen, J.Q. Wang, J.M. Wang, J. Wang, Investigation of various Pd species in Pd/BEA for cold start application, Catalysts 9 (2019) 10.

[60] A.M. Beale, B.M. Weckhuysen, EXAFS as a tool to interrogate the size and shape of mono and bimetallic catalyst nanoparticles, Phys. Chem. Chem. Phys. 12 (2010) 5562–5574.

[61] K. Murata, Y. Mahara, J. Ohyama, Y. Yamamoto, S. Arai, A. Satsuma, The metal-support interaction concerning the particle size effect of Pd/Al$_2$O$_3$ on methane combustion, Angew. Chem. Int. Ed. 56 (2017) 15993–15997.

[62] J.J. Willis, A. Gallo, D. Sokaras, H. Aljama, S.H. Nowak, E.D. Goodman, L. Wu, C.J. Tassone, T.F. Jaramillo, F. Abild-Pedersen, M. Cargnello, Systematic structure–property relationship studies in palladium-catalyzed methane complete combustion, ASC Catal. 7 (2017) 7810–7821.

[63] A.Y. Stakheev, A.M. Batkin, N.S. Teleguina, G.O. Bragina, V.I. Zaikovsky, I.P. Prosvirin, A.K. Khudorozhkov, V.I. Bukhtiyarov, Particle size effect on CH$_4$ oxidation over noble metals: comparison of Pt and Pd catalysts, Top. Catal. 56 (2013) 306–310.

[64] C.A. Muller, M. Maciejewski, R.A. Koeppel, R. Tschan, A. Baiker, Role of lattice oxygen in the combustion of methane over PdO/ZrO$_2$: combined pulse TG/DTA and MS study with O-18-labeled catalyst, J. Phys. Chem. 100 (1996) 20006–20014.

[65] C.A. Müller, M. Maciejewski, R.A. Koeppel, A. Baiker, Combustion of methane over palladium/zirconia: effect of Pd-particle size and role of lattice oxygen, Catal. Today 47 (1999) 245–252.

[66] International Zeolite Association, Structure Commission, http://www.iza-structure.org/ (Accessed April 2020).